Experimental Investigations of Optimized 3D Printing Planar X-joints Manufactured by Stainless Steel and High-strength Steel

Senbin Huang[a], Xiaowei Deng[a,*], Yuhang Wang[b]

[a]*Department of Civil Engineering, University of Hong Kong, Pokfulam, Hong Kong*
[b]*School of Civil Engineering, Chongqing University, Chongqing 400045, PR China*

Abstract

Welded joints are often employed in high-rise buildings and grid-shell structural systems but on-site welding of cut steel tubes for spatially complex frame systems is problematic, time consuming and difficult to ensure quality. Innovative prefabrication combining topology optimization (TO) using the Solid Isotropic Material Penalization Method (SIMP) and additive manufacturing (AM) provides an innovative solution for materially efficient mass production of repetitive joints. Optimized AM joints can be bolted to other members on-site, which promotes construction efficiency, and overcomes the barriers of on-site welding. In this paper, tensile tests are conducted to assess the material properties of mild and stainless steels materials used in different manufacturing processes. Welded and 3D printed joints using different materials are then investigated to maximize the mechanical properties by taking full advantage of AM and TO. A customized non-contact 3D-DIC (Digital Image Correlation) technique based on an open source tool (MultiDic) is applied to analyze and visualize the strain distribution in planar tubular and topologically optimized joints. AM joint exhibits a uniform stress distribution which avoids stress concentrations and the innovative configuration of the optimized joint has good energy absorption resulting in the protection of the central core region of the joint.

Keywords: Topology optimization (TO), Additive manufacturing (AM), 3D Digital Image Correlation

*Corresponding author. E-mail: xwdeng@hku.hk; Phone: +852 2859 1974

(3D-DIC), Stainless steel, High-strength mold steel

1. Introduction

In high-rise buildings and grid-shell construction schemes, welded joints have been commonly implemented. The traditional complex multi-planer steel joint is produced through on-site welding steel tubes together, which demands high-precision manufacturing and installation. Furthermore, since residual stresses are generated after the joints cool down which can lead to local damage, and the welding quality depends heavily on individual skill proficiency and the technical expertise of each welder, the reliability of the on-site welding quality for the core joints of large span space frame structures cannot be easily guaranteed. Steel joints capable of achieving both good continuity and sufficient strength between adjacent modules for on-site assembly are a critical issue in steel construction design. Currently, common methods of enhancing the strength of structural steel joints are mainly through localized reinforcement of the wall thickness of the joint [1, 2]. Reinforcement methods such as internal concrete filling [3], internal and external stiffener rings [4–6] and external fiber reinforced polymer composite reinforcement [7] and manufacturing with high-strength steel can be employed to optimize the performance of the joints without changing the failure modes. Costs are incurred during the curing of concrete, as well as the installation of internal and external reinforcement ribs and fiber-reinforced polymer composite reinforcement. Mild steel is widely used in engineering because of its low cost and weldable and machinable properties, and however the iron in mild steel can oxidize if it is not properly coated. Stainless steel is an iron alloy resistant to rusting and corrosion, and 316L stainless steel is a very common material for additive manufacturing. Because of the mechanical properties, as well as their economy and sustainability, high strength steels are appropriate for structural applications [8, 9]. High-strength steels have a substantially higher yield strength than conventional mild steels, allowing them to withstand larger loads with significantly

smaller cross-sectional dimensions of the members under the same design circumstances, reducing dead loads and construction costs. Some obstacles or constraints remain in the practical application and design of high-strength steel structures, such as consistent welding quality, fracture resistance under low cyclic fatigue loading, etc. Because of inconsistent weld quality and fracture resistance under adverse mechanical fatigue loads, high-strength steels do not constitute the ideal structural material for every design circumstance [10]. Therefore, there is a demand for a new type of joint that can not only replace the traditional welded joints to avoid on-site welding but also transfer the damage region to change the failure modes resulting in overcoming the difficulties of reinforcement and maintenance. Shi [11] proposed a novel casting joint, which uses bolts to connect structural members for convenient installation, and studied the mechanical properties and failure mechanism through experimental and numerical analysis. Mass production of repeated units is generally efficient; casting many different types of joints and fabricating various high-precision molds can be expensive and time-consuming.

Topology optimization (TO) is a type of structural optimization method that finds the ideal material configuration inside a particular design region for a given combination of loads, boundary conditions, and constraints. It is extensively applied to various architecture and engineering [12], vehicles [13], and aerospace [14–17]. Xie [18] first proposed the evolutionary structural optimization method (ESO) by gradually removing inefficient materials until the specified material volume requirements are satisfied. However, it is difficult to converge to obtain an effective solution in some cases. Bendose [19] introduced density functions to transfer discrete optimization problems to continuous problems, mainly applied to solve engineering problems because of their simple form. Topologically optimized structures with arbitrary configurations are not easily fabricated using traditional manufacturing methods, therefore a novel additive manufacturing technique can generate innovative configurations by fabricating joints layer by layer, providing a significant potential to optimize joint performance.

Additive manufacturing (AM), commonly referred to as 3D printing, is expected to revolutionize the way structures are designed and fabricated [20]. Ribeiro [21] analyzed the application of topology optimization in engineering, presenting some engineering cases [22–25] in recent years with the combination of topology optimization and additive manufacturing. AM has the following advantages over traditional machining and casting techniques; AM extracts continuous cross-sectional layers based on resolution directly from the digital file of the model and manufactures them layer by layer, allowing direct fabrication when the file of the 3D model is obtained. While traditional manufacturing methods have limitations on the geometric characteristics of the model, such as casting methods that rely on the proper draft angle, AM can produce parts with arbitrary geometric configurations. And AM does not require continuous manipulation and unique clamping by specialized technicians compared to subtractive manufacturing techniques that include milling and cutting [26]. The main limitations of AM are the relatively slow manufacturing speed and the higher total cost compared to conventional techniques. However, as the technology develops, the cost will gradually decrease in the future. AM plays an outstanding role in advanced manufacturing for its powerful individual manufacturing capabilities [15, 27–29]. AM enables the selectivity of different materials so that the use of materials can be customized to achieve optimal outcomes for different design requirements. Common materials that can support 3D fabrication include titanium alloy powder, stainless steel alloy powder, martensitic powder, nickel high-temperature alloy powder, etc. However, there is limited research on the applicable metallic materials for AM with optimized joints. The analysis of joints produced by various production methods involving various materials might benefit from AM to enhance structural performance. The potential of TO and AM is fully implemented to explore more advanced design methods to fabricate efficient and innovative structures.

Conventional contact experimental measurements are less applicable to optimized results for complex geometric configurations after optimization. DIC (Digital Image Correlation) is a non-contact optical dig-

ital technology that analyzes changes in surface strain within a material's region of interest (ROI) based on the existence of natural or synthesized speckle patterns on the material's surface [30–32]. DIC matches the corresponding set of pixels around the ROI of different images and calculates the deformation and strain of the corresponding set of pixels in a given target image. The potential of DIC to quantify massive deformations across a large field without contact makes it a preferred approach for materials characterisation [33–35] and is frequently applied in various geometry and strain measurements in the biomedical applications [36–40]. Some researchers have investigated the mechanical properties and microstructure of tensile coupons using the wire arc additive manufacturing (WAAM) method combined with DIC [41–43]. In this paper, a customized 3D-DIC solution based on an open source tool (MultiDic) for the optimized AM steel joints experiments is presented and validated with the numerical simulation, which fills the gap in the novel non-contact experimental method based on topologically optimized steel joints.

The paper will be divided into the following sections illustrated in Fig. 1. The Solid Isotropic Material with Penalization (SIMP) approach is employed in this paper to optimize the design of the tubular X-joints. In the post-processing stage of the original optimized model, it is necessary to use computer-aided design software (*Rhinoceros*) to improve its uniformity and fabrication-friendliness by addressing issues such as internal holes, rough surfaces, and irregular shapes. Subsequently, tensile tests are conducted to evaluate the properties of materials such as mild steel, stainless steel, and high-strength mold steel that have been produced using various manufacturing techniques including welding and 3D printing. In compression tests, 2D and 3D-DIC are utilized to analyze the strain and deformation of tubular and optimized joints, which are validated through numerical simulations. These tests provide essential criteria for future material selection in the additive manufacturing of optimized steel joints and serve as a reference for future experimental design.

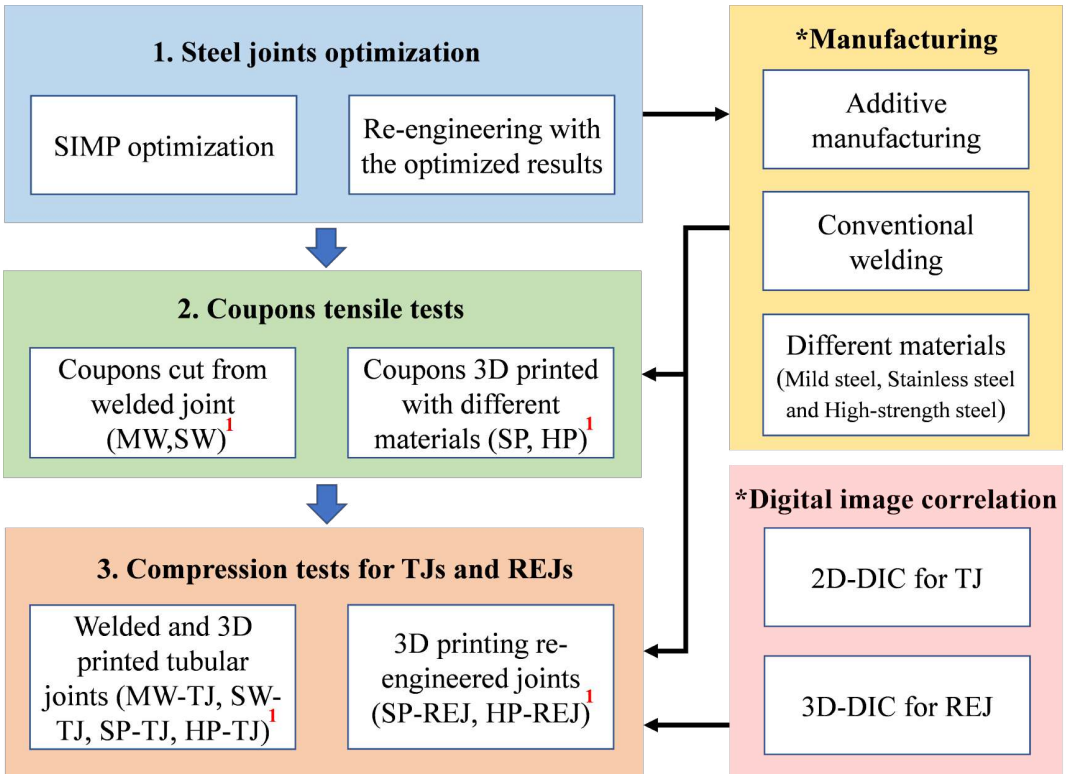

Figure 1: Diagram of topology optimization for steel joints.[1]

2. Methodology

2.1. Numerical techniques

The Solid Isotropic Material with Penalization (SIMP) method is implemented in this paper to modify the relative density of each element in order to acquire the optimal subset of materials and the stiffer joint. The density-based optimization method assigns Young's modulus E_e based on the relative density x_e of each element e which is continuous between 0 and 1. The material's power-law interpolation function is demonstrated valid as long as specific requirements are met, such as the penalty factor $r = 3$ [44].

$$E_e = E_{min} + x_e^r(E_0 - E_{min}), \quad x_e \in [0, 1] \tag{1}$$

[1] Abbreviations are listed in Appendix A

where E_0 is the Young's modulus of steel; E_{min} is the assigned minimum stiffness to avoid singularities in the matrix calculation. The objective function c is the inverse of the stiffness. The following equations outline the optimization problem:

$$
\begin{aligned}
Find &: \boldsymbol{x} = \{x_1, x_2, x_3, ..., x_e\}^T \in \boldsymbol{R}^n, e = 1, 2, 3, ..., N \\
Min &: c = \boldsymbol{U^T K U} = \sum_{e=1}^{N} \boldsymbol{u_e^T k_e u_e} = \sum_{e=1}^{N} (x_e)^r \boldsymbol{u_e^T k_0 u_e} \\
Subject\ to &: \boldsymbol{KU} = \boldsymbol{F} \\
&\alpha \cdot V_0 = \sum_{e=1}^{N} x_e v_e \leq V^* \\
&U_{max} < U^* \\
&S_{max} < S^* \\
&0 < x_{min} \leq x_e \leq x_{max} \leq 1
\end{aligned} \tag{2}
$$

where x_{min} and x_{max} are the minimum and maximum limit of the relative element density, respectively; the number of discrete elements in joint is N, and elemental volume is v_e; $\boldsymbol{u_e}$ represent the elemental vector of deformation and $\boldsymbol{k_0}$ denotes the stiffness matrix; and U^* and S^* indicate the maximum limits of the displacement and stress, respectively. α is the volume ratio between the target volume V^* and the initial volume of design domain V_0. Sigmund [45, 46] proposed filtering techniques to avoid the checkerboard configuration in TO. As demonstrated below, the density filter [47] is implemented to assess the modified elemental density $\widetilde{x_e}$:

$$
\widetilde{x_e} = \frac{1}{\sum_{i=1}^{N} H_{ei}} \sum_{i=1}^{N} H_{ei} x_i \tag{3}
$$

where $H_{ei} = r_{min} - dist(e,i)$ and r_{min} is filter radius; The distance between elements e and i is specified as $dist(e,i)$. To acquire the optimum geometric configuration, the solid X-joint is employed as a design domain for optimization Fig. 2. In this paper, the optimization module of the commercial software ABAQUS 6.13 is applied for topology optimization, and the element type is the 10-node quadratic tetrahedron (C3D10).

In this paper, the chord length, two vertical brace lengths are arranged as 200 mm and 80 mm, respectively, to avoid that the interaction region of the horizontal chord and the vertically connected braces can resist all the deformations during vertical loading, according to the related research from Madhup [48], Zhu [5] and Feng [49].; and the tubular wall thickness is set as 2 mm. Lan [50] compared the effects of different modeling features on the optimization results and found that the presence or absence of a weld did not affect the ultimate strength. Therefore, the modeling simplifies the weld seam to a 2 mm fillet. The external forces and constraints for the solid and tubular joints are applied in four 2 mm wide annular regions at the ends. The deformation constraints are applied in these regions without limiting in the normal direction. The pressure of 70 MPa is normally applied inward to these four end planes, which is less than the joint resistance obtained by CIDECT [51] and EC3 [52]. The volume ratio constraint is arranged as 21%. The optimized joints are not directly applicable for additive manufacturing since the irregular and rough geometric features and, therefore, the joints need to be re-engineered.

The stress and strain contour plots for tubular joint and the optimized joint after re-engineering under same boundary conditions are presented in Fig. 3. After topology optimization, the load transmission paths of the joints are more clear and direct, and the distribution of stress is uniform in the optimized joints to eliminate the stress concentration at the chord and braces connected region of the tubular joints. The maximum deformation and stress still meet the constraints while the maximum stress is decreased nearly 60 %, which indicates that the optimized joint is stiffer than tubular joint.

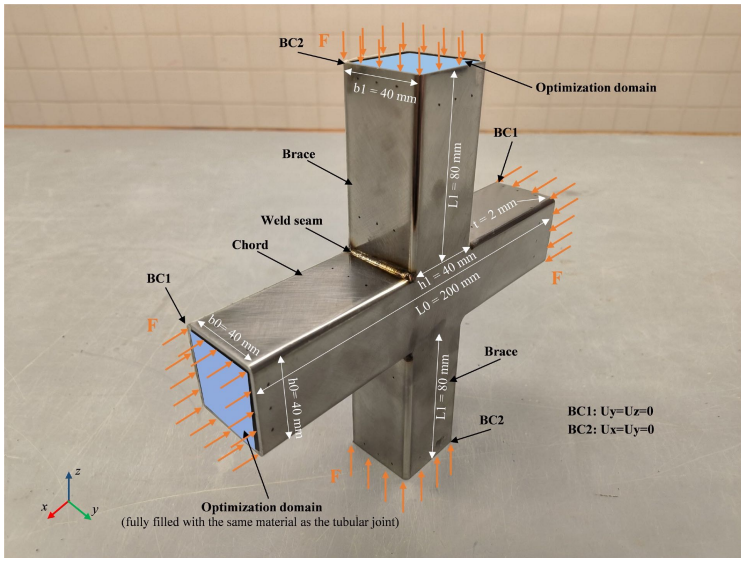

Figure 2: Dimension and boundary conditions of tubular joint.

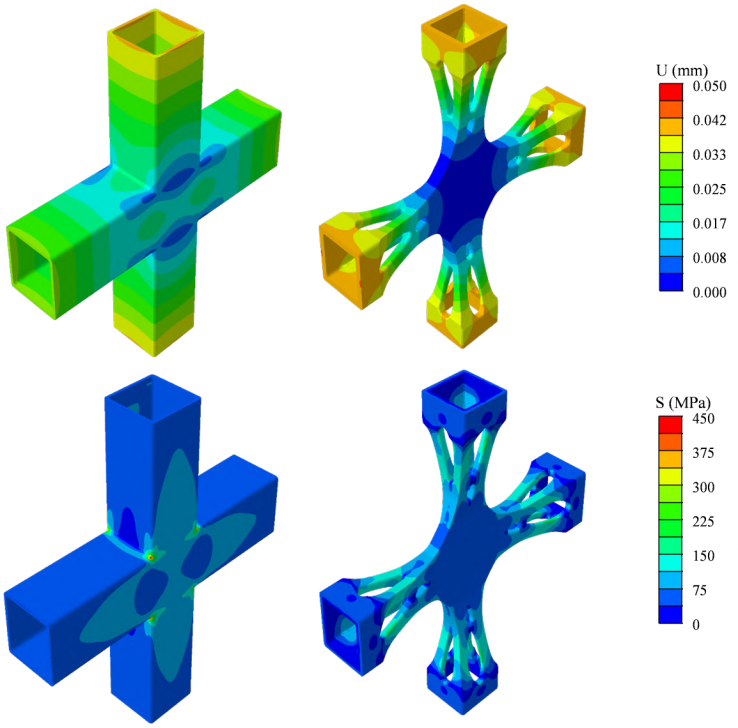

Figure 3: Contour plots of deformation and stress between tubular joints and optimized joints.

2.2. Digital image correlation method (2D/3D-DIC)

DIC provides global strain distribution at the macroscopic level. Depending on the different camera views and the relative magnitude of deformation in directions other than in-plane, 2D and 3D-DIC are implemented to detect strain in planes and stereo, respectively [53]. Traditional measuring methods are no longer feasible for field testing of novel optimized steel joints related to the arbitrary geometrical characteristics produced following topology optimization. To investigate the strain distribution in complex spatial steel joints more intuitively, the open-source single-view 2D and multi-view 3D digital image correlation toolboxes [31, 54] are used as the assistant experimental methods to measure the strain distribution during compression tests accurately. The effectiveness of DIC has also been verified [55, 56]. The entire frame is assembled with five aluminum extruded tubes (2020L) and designed with laser-cut acrylic plates on the base of the loading machine. At the same time, customized additive manufactured resin connectors are applied to ensure the stability of the frame. Three sets of Raspberry V2 cameras and the 4B motherboards are mounted on the same acrylic plate to capture images. The focal points of the three cameras are overlapping and at an angle of 10° to each other in the horizontal plane. In contrast to 2D-DIC, which obtains image sequence of a deformed planar pattern basing one camera, stereo 3D-DIC acquires images of a deformed irregular surface using multiple cameras [57]. 2D-DIC is preferred when the deformation towards the outer surface is small, while stereo 3D-DIC is usually adopted to measure 3D multi-planar deformation [58] accurately. The field of view (FOV) depends on the angle of two cameras, and a high correlation coefficient results in significant errors when the FOV is large. The camera in the middle, accompanied by 2D-DIC is applied for non-contact measurement of the tubular joints. In contrast, the camera pair with an angle of 20° degrees on both sides combined with 3D-DIC is adopted to measure the strain of the optimized joint after re-engineering with higher accuracy. These three Raspberry Pi cameras are manually set to the same exposure combination parameters such as shutter speed, aperture, ISO

sensitivity, and white balance for each experimental sample to facilitate post-processing and guarantee the quality of the images. A network switch connects the three Raspberry Pis and the host computer for real-time communication. During the compression test, a DC-driven wrap-around LED strip was applied to supplement sufficient illumination and reduce surface reflections to prevent effective post-processing. Furthermore, a black curtain surrounding the entire experimental set-up absorbed the ambient reflected light. A photo sequence is captured at 15-second intervals. As demonstrated in Fig. 4, speckles with a size of 3-8 pixels are randomly sprayed on one side of the tubular joints and the optimized joints. A LVDT (linear variable differential transformer) is mounted in the middle of the opposite side to monitor horizontal deformation.

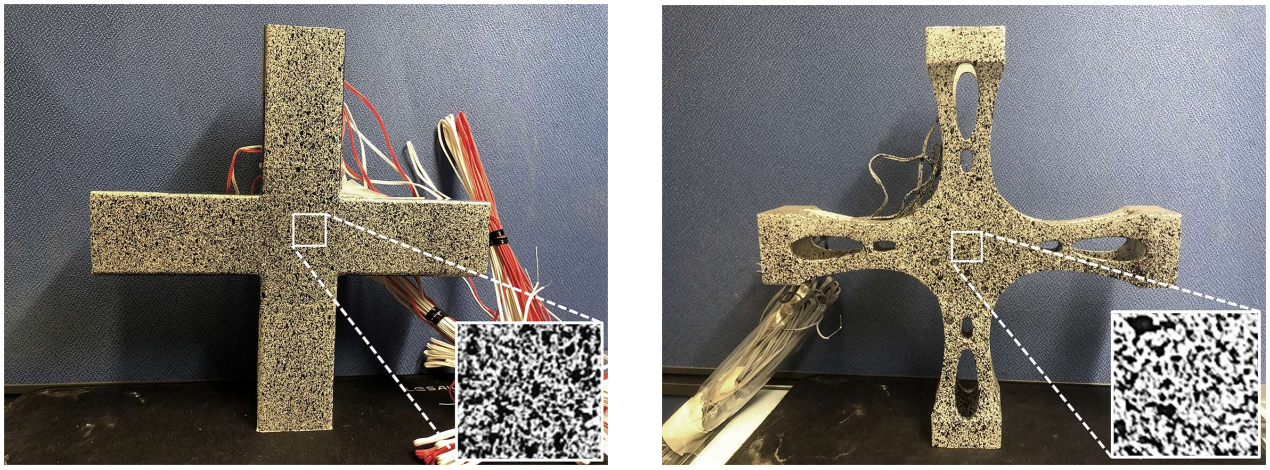

(a) Speckle pattern of TJ

(b) Speckle pattern of REJ

Figure 4: Speckle patterns of TJ and REJ.

The non-contact 3D-DIC experimental procedure is organized into four steps. First, the aberrations of each camera lens are calibrated using a calibration object with black and white checkerboard images. Second, the calibration object with accurate spatial coordinates of each grid point is employed to calibrate the image points using the direct linear transformation method (DLT)[31, 59]. After that, 2D-DIC analysis is performed by dividing the same region of interest for each image sequence. Eventually, spatial

reconstruction is carried out with the 2D-DIC results and the calibration. The loading rate of the loading machine remains 0.5 mm/min, while two cameras with an angle of 20° are engaged for taking image sequences simultaneously at an interval of 15 seconds by 3D-DIC.

To map 2D results to stereo results, a direct linear transformation (DLT) is required; this DLT relies heavily on an idealized camera without distortion [31]. The difference between the before and after calibrated images indicates that the adjustment for distortion increases in the direction of radiation from the center of the lens to the edge. After removing the distortion, the camera pair must be converted between planar image points and global spatial points according to the DLT algorithm. A cylindrical calibration object and a custom-designed vase object in Fig. 5 manufactured by 3D printing are applied to obtain the transformed mapping relationship from planar to spatial points. The 2D-DIC is performed separately for the image sequences taken by each camera; after that, the results of 2D-DIC are transferred to that of 3D-DIC according to the coordinate transformation relationship obtained by DLT.

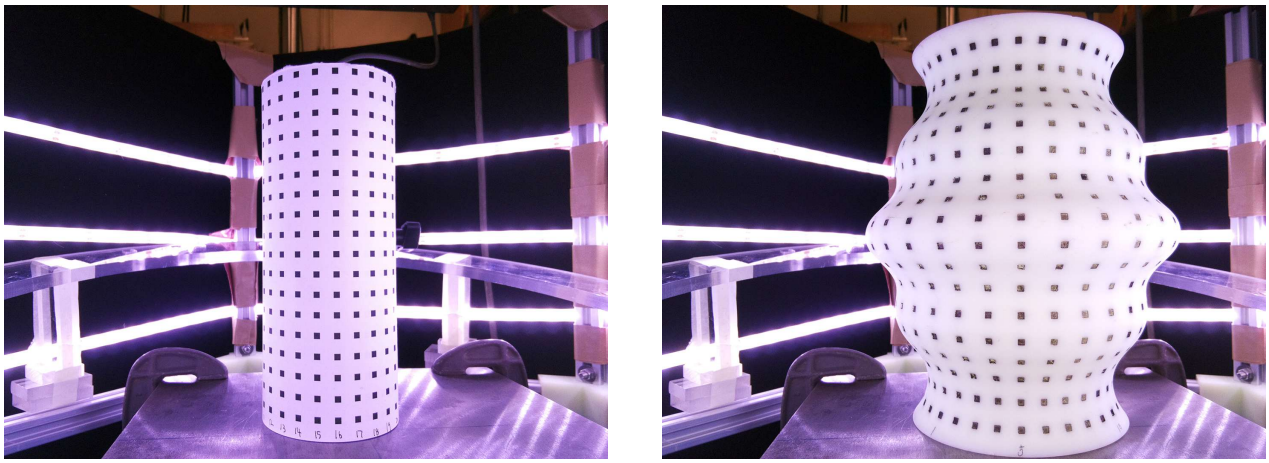

(a) Cylindrical object (b) Vase object

Figure 5: Calibration objects for DLT.

3. Experimental schemes

3.1. Specimen manufacturing

All 3D printed joints are fabricated by selective laser melting (SLM) technique [60] with a FS271M machine from manufacturing company FARSOON equipped with a 500W laser. And the simplified workflow of the manufacturing process is shown in Fig. 6. The build chamber is available in sizes up to $275 \times 275 \times 320\ mm^3$ and can be manufactured with an accuracy of 0.02 *mm* for each printing layer. The tubular joints being tested in this experiment are currently divided into mild steel welded joint (MW), stainless steel welded joint (SW), 3D printed stainless steel joint (SP), and 3D printed high-strength mold steel joint (HP) based on material and fabrication differences. MW and SW are the most common construction materials. MW has poor corrosion resistance but the lowest cost, SW has better ductility than MW and is less susceptible to corrosion. SP and HP are well established and widely used in 3D printing. SP has good corrosion resistance and ductility, while HP is widely used in mold making for high yield strength. For the welded joints, the coupons are cut directly from the same batch of steel tubes, The chemical material composition of the different groups provided by the suppliers is shown in the Tab. 1. The joints and coupon fabricated by different manufacturing techniques and materials for compression and tension tests are shown in the Fig. 7.

Table 1: Chemical material composition.

(%)	C	Si	Mn	P	S	Nb	V	Ti	Cr	Ni	Mo
MW	0.130	0.160	0.380	0.020	0.027	0.019	0.022	0.020	0.021	0.019	0.018
SW	0.028	0.450	1.170	0.025	0.017	-	-	-	17.120	13.880	2.000
SP	0.030	1.000	2.000	-	-	-	-	-	16∼18	10∼14	2∼3
HP	0.400	1.050	0.430	-	-	-	1.140	-	4.990	-	1.300

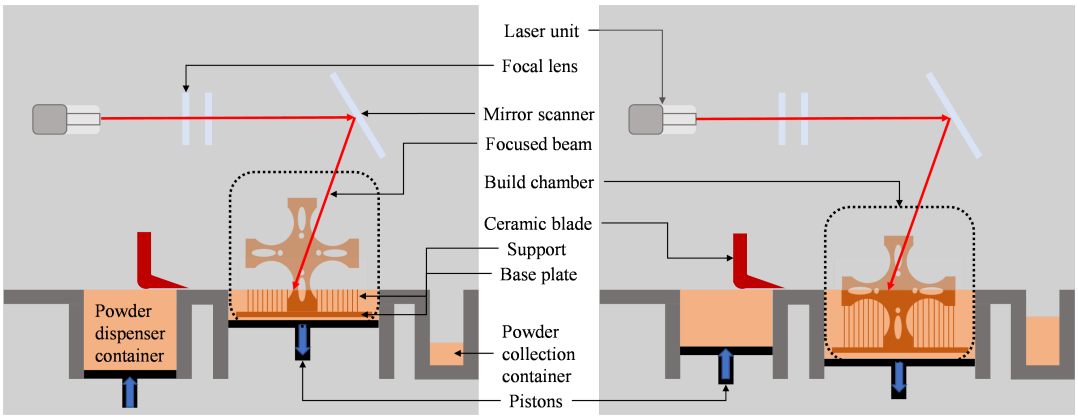

Figure 6: The manufacturing process of the optimized joint.

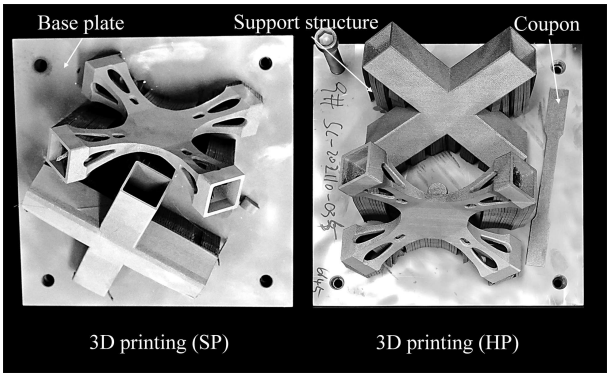

(a) Before removing the support structure.

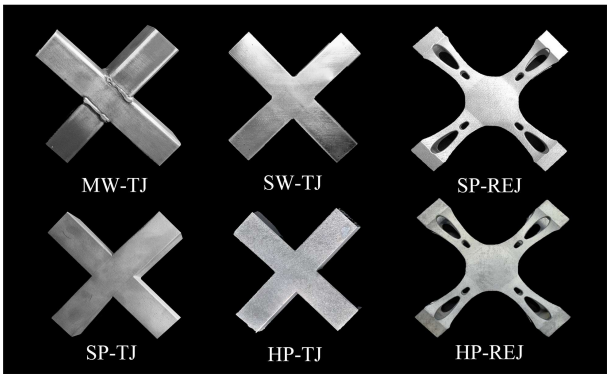

(b) After removing the support structure.

Figure 7: Specimens for the compression tests.

3.2. Setup of tensile test

Specimens are tested in tension to determine the impact of various material properties and manufacturing techniques. There is a total of 16 sheet-type specimens (4 SP, 4 SW, 4 MW, and 4 HP) based on ASTM-E8[61], and the Fig. 8 and Tab. 2 illustrate the dimensions of specimens before tension. Huang [53] presents that the material characteristics of 3D printing coupons differ relying on the printing orientation. MW and SW are cut from the corresponding welded tubular joints, respectively, while SP and HP are 3D printed with stainless and high-strength steel materials accordingly. In this study, all coupons and joints are printed with the same orientation to guarantee the same material properties to take into account the cost of production time and workload of post-processing, as well as to guarantee manufacturing accuracy.

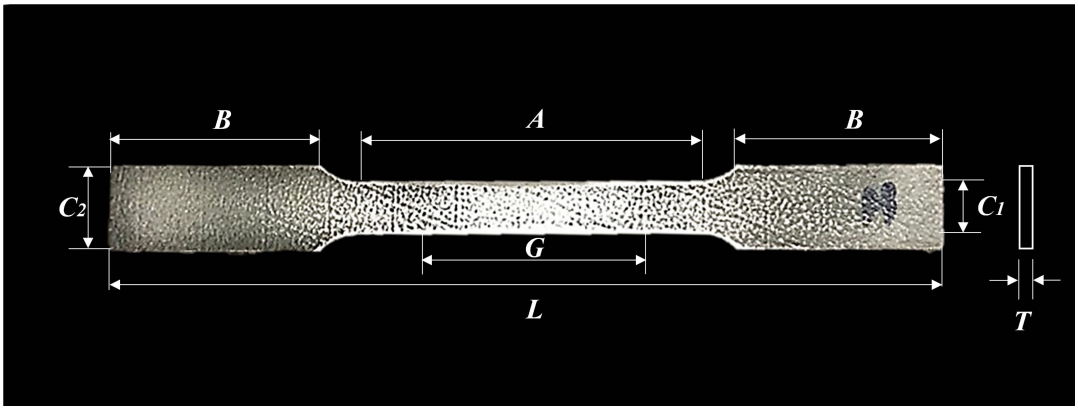

Figure 8: Sheet-type tensile test specimen.

For the elastic stage, the average value of two strain gauges (SG) mounted at the two centers of each specimen is employed, whereas for the plastic stage, the extensometer is applied. The MTS 50 kN loading device is employed, and loading rates of 0.05 mm/min and 0.8 mm/min are adopted when the strain is before and after 0.6%, respectively. The setup for the tension test is shown in Fig. 9.

Table 2: Dimensions of the tested coupons (mm).

Coupons	G	C_1	T	R	L	A	B	C_2
MW-1	50	12.48	2.06	12.5	196	57	49	19.96
MW-2	50	12.50	2.06	12.5	198	57	50	19.98
MW-3	50	12.46	2.10	12.5	194	57	49	19.92
MW-4	50	12.46	2.08	12.5	196	57	50	19.96
SW-1	50	12.58	1.90	12.5	198	57	50	20.04
SW-2	50	12.56	1.90	12.5	200	57	49	20.02
SW-3	50	12.54	1.90	12.5	198	57	50	20.06
SW-4	50	12.60	1.90	12.5	199	57	50	20.00
SP-1	50	12.50	2.24	12.5	200	57	50	20.00
SP-2	50	12.52	2.10	12.5	200	57	50	20.00
SP-3	50	12.52	2.74	12.5	199	57	50	20.00
SP-4	50	12.50	2.72	12.5	199	57	50	20.00
HP-1	50	12.56	1.70	12.5	200	57	50	20.00
HP-2	50	12.50	1.50	12.5	200	57	50	20.00
HP-3	50	12.54	1.98	12.5	200	57	50	20.00
HP-4	50	12.50	1.96	12.5	200	57	50	20.00

[1] **Note**: G: Length of gauge; A: Length of test region; C_1: Width of test region; T: Thickness; R: Radius of the end fillets; L: Total length; B: Gripping length; C_2: Gripping width.

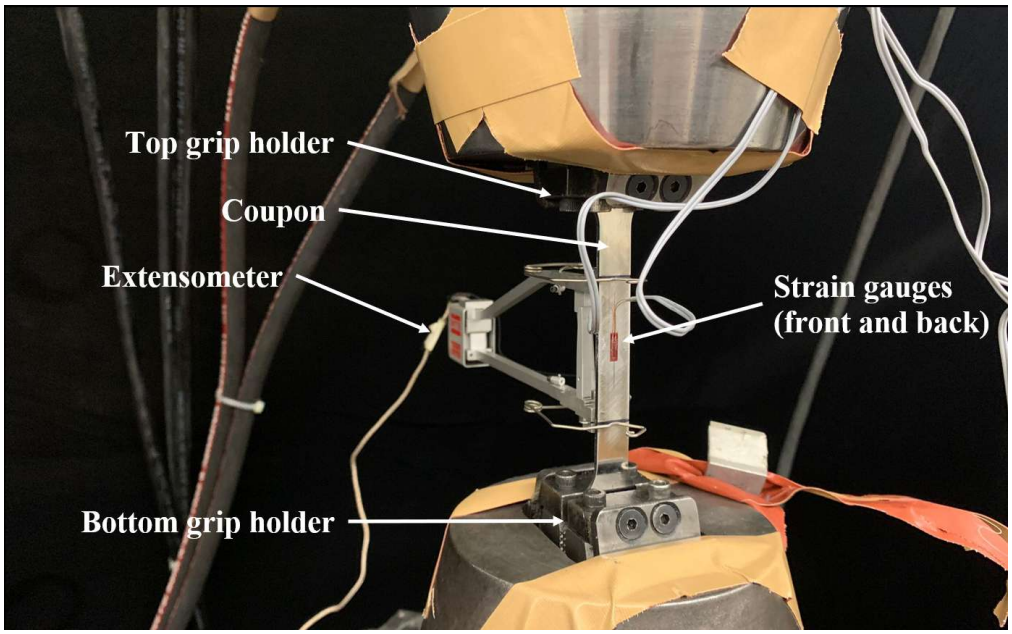

Figure 9: Setup of the tension test.

3.3. Setup of compression test

The loader is a hydraulic testing machine with a servo control capacity of 1000 kN. On top of the loader, a ball bearing is installed, and the top solid steel plate could be adjusted to eliminate eccentric loading. Displacement is controlled at a rate of 0.5 mm/min until the maximum limit is achieved, which is 15 mm. There are six specimens for compression tests, including MW-TJ, SW-TJ, SP-TJ, HP-TJ, SP-REJ, and HP-REJ, while TJ and REJ are the abbreviations of tubular and re-engineered joints, respectively. The dimensions of the specimens and the materials employed as well as the test setup are shown in Tab. 3 and Fig. 10, respectively.

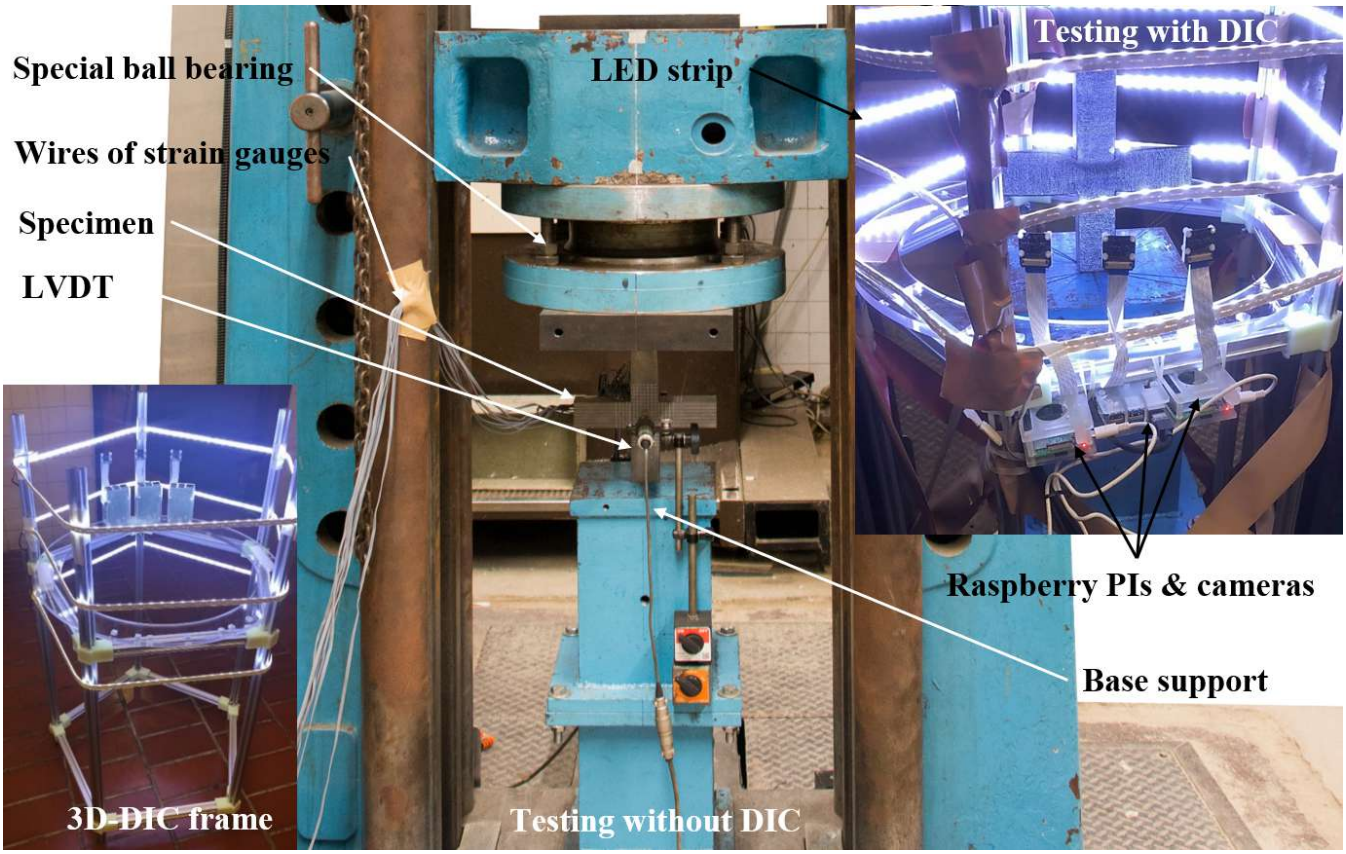

Figure 10: Setup for the compression test.

Four strain gauge rosettes are mounted at the critical positions of the tubular joints to obtain the maximum and minimum principal strains. SG1 is attached at the center of the chord, while SG2, SG3,

Table 3: Specimens for the compression tests.

	b_1 (mm)	h_1 (mm)	b_0 (mm)	h_0 (mm)	L_1 (mm)	L_0 (mm)	Material	Manufacturing
MW-TJ	40	40	40	40	80	200	Mild steel	Welding
SW-TJ	40	40	40	40	80	200	Stainless steel	Welding
SP-TJ	40	40	40	40	80	200	Stainless steel	3D printing
HP-TJ	40	40	40	40	80	200	High-strength mold steel	3D printing
SP-REJ	40	40	40	40	80	200	Stainless steel	3D printing
HP-REJ	40	40	40	40	80	200	High-strength mold steel	3D printing

[1] **Note**: b_1: Brace width; b_0: Chord width; h_1: Brace height; h_0: Chord height; L_1: Brace length; L_0: Chord length.

and SG4 are installed close to the weld seam with the distance of 5 mm; the locations for installing strain gauges on the tubular and re-engineered joints are shown in the Fig. 11.

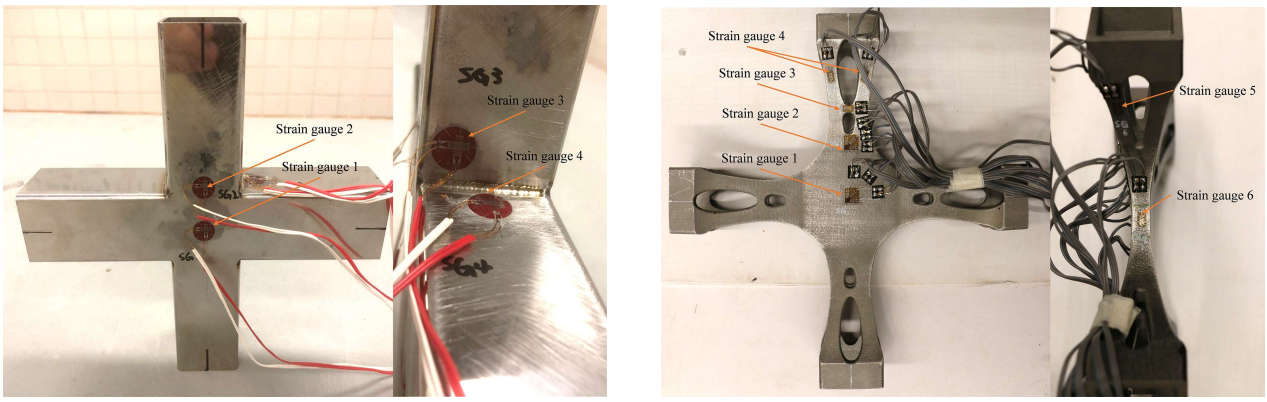

(a) Strain gauges of tubular joint.

(b) Strain gauges of re-engineered joint.

Figure 11: Layout of strain gauges.

4. Experimental results

4.1. Material tensile tests

220 To minimize overestimation of material strength and for research purpose, the loading of the specimens was held for 1 minute and 40 seconds to get static curve of strain-stress relationship according to Huang's related work [62]. Some cases of these four materials are presented in Fig. 12.

The outliers from the normally distributed population are expected to be excluded by adopting Grubbs's

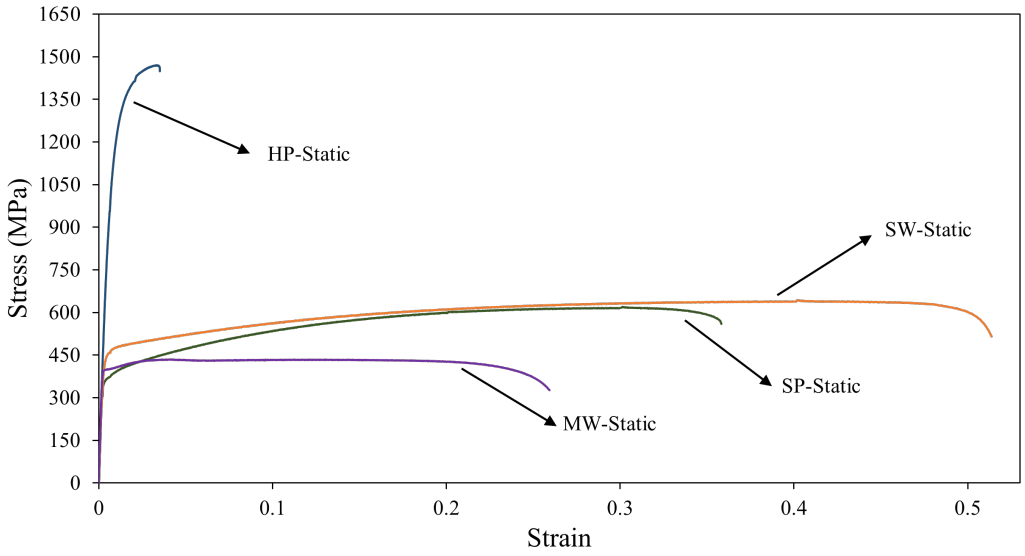

Figure 12: Dynamic and static stress-strain relationship of steel coupons.

Table 4: Tensile test results in material properties.

By welding	MW-1	MW-2	MW-3	MW-4	SW-1	SW-2	SW-3	SW-4
Yield Strength (MPa)	355.64	344.91	400.64	398.20	446.26	446.28	448.81	418.89
Ultimate Strength (MPa)	399.39	380.84	440.27	434.78	630.95	638.62	636.24	627.74
Young's Modulus (GPa)	207.05	170.87	206.44	221.64	184.41	181.27	180.68	173.06
Strain at Fracture	0.0835	0.1677	0.2571	0.2593	0.5510	0.5655	0.5625	0.5648
By 3D printing	SP-1	SP-2	SP-3	SP-4	HP-1	HP-2	HP-3	HP-4
Yield Strength (MPa)	362.23	356.89	382.92	397.80	1096.32	1104.52	1001.01	972.45
Ultimate Strength (MPa)	619.86	597.03	612.28	630.72	1474.90	1470.12	1345.28	1394.77
Young's Modulus (GPa)	187.64	186.46	183.04	190.80	200.47	198.13	192.99	183.23
Strain at Fracture	0.3582	0.3539	0.3904	0.3737	0.0355	0.0351	0.0332	0.0368

test, and the box plots obtained are displayed in Fig. 13 and the results collated after removing the outliers are shown in Tab. 5. MW seems unstable, and the variance of material properties is larger for each test compared to SW. Following the supplier's chemical composition table (Tab. 1), the low nickel level reduces the material's corrosion resistance and increases the possibility of surface rusting, and it is challenging to maintain the material's stability during manufacturing. SW and SP are both formed of stainless steel; SW is created by cutting cold-rolled stainless steel tubes, whereas SP is made additively by laser melting stainless steel powder. In comparison to MW, SW has the most stable material qualities and is excellent for welding, whereas HP has the smallest fracture strain and the largest ultimate strength and yield strength; consequently, brittle failure can easily occur. Young's modulus of MW is the largest among these four materials. The variance of the strain at fracture is large for MW and is influenced by factors such as different product batches, local variations in thickness and strength of the specimen due to rusting, etc.

Table 5: Material properties of different groups.

Group	MW	SW	SP	HP
Yield strength (MPa)	374.85	447.11	374.96	1043.57
Ultimate strength (MPa)	413.82	633.39	620.95	1421.27
Young's modulus (GPa)	211.71	182.12	186.98	197.20
Fracture strain	0.1919	0.5642	0.3619	0.0358

4.2. Strain distribution

4.2.1. 2D-DIC for tubular joints

The tubular joints involved in the compression tests consist of four types: MW-TJ, SW-TJ, SP-TJ, and HP-TJ. The first two types, MW-TJ and SW-TJ, are obtained by cutting the square tubes of both mild steel and stainless steel into two 80 mm braces and welding them on both sides of a 200 mm chord.

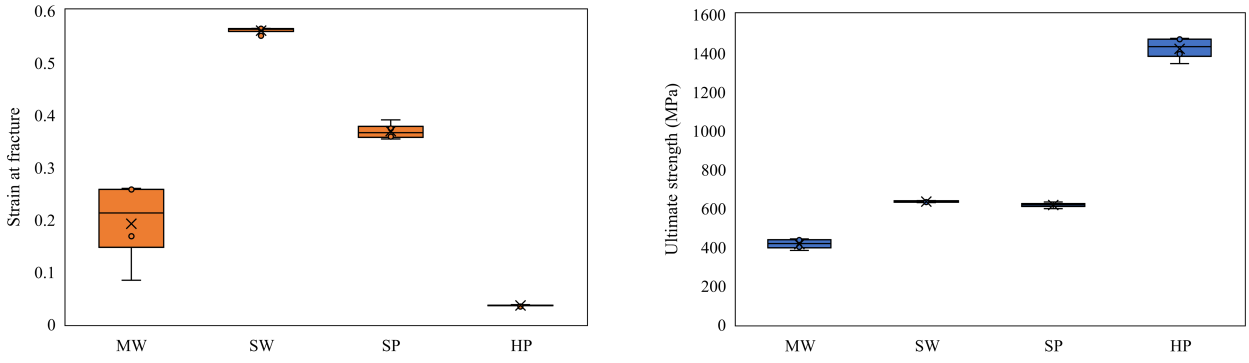

(a) Fracture strain

(b) Ultimate strength

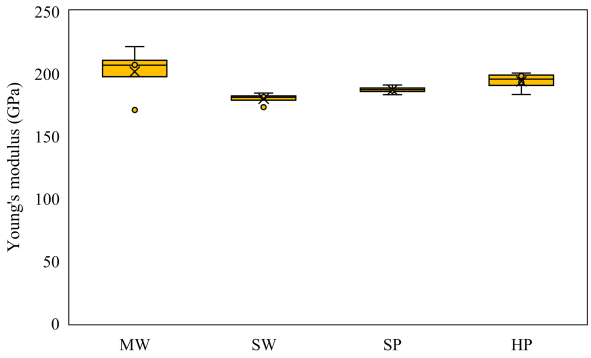

(c) Young's Modulus

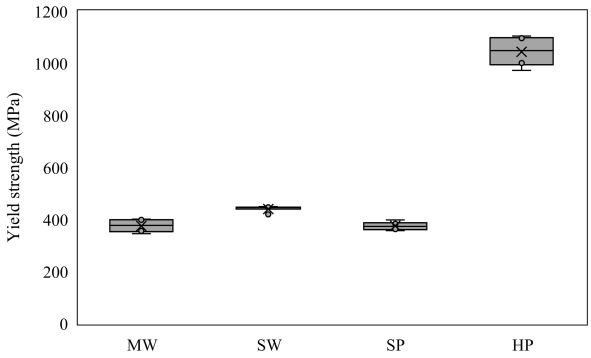

(d) Yield Strength

Figure 13: Box plots about material properties.

SP-TJ and HP-TJ are obtained by 3D printing with stainless steel powder and HP powder. Two separate suppliers weld MW-TJ and SW-TJ, and the thickness of the MW-TJ weld throat is more than that of SW-TJ, as indicated in Fig. 14. The loading rate for all tubular nodes is 0.5 mm/min and will stop when the vertical displacement reaches 16 mm. 2D-DIC is preferable for non-contact strain measurement since the surface of the tubular joint is flat. When the vertical displacement is close to 4 mm, the MW-TJ initially cracked; therefore, the corresponding strains of SW-TJ, SP-TJ, and MW-TJ were extracted for analysis. However, HP-TJ suddenly cracked and failed only when the vertical displacement was 2.64 mm. When the displacement in vertical compression is 4.13 mm, the numerical simulation of the tubular joint for the compression test, based on the material properties of stainless steel obtained in the tensile test of the specimen, is quite similar to the results of 2D-DIC, proving the validity of the 2D-DIC non-contact measurement. Although 3D printing can guarantee the accuracy and quality of the joints during additive manufacturing as much as possible, post-processing such as annealing, grinding, etc. cannot prevent the introduction of initial imperfections to the structure, which could result in sudden damage and failure. All the results are shown in Fig. 14.

When compression exceeds the same level, the maximum compression strain in additively manufactured joints is less than that in welded joints. Because residual stresses are introduced at the weld seam of welded tubular joints, additive manufacturing technologies can effectively regulate the precision of the joint through reducing the weld seam. Stainless steel is less prone to crack generation than mild steel and HP, and HP is less suitable for tubular joints because of its lower load-carrying capacity and sudden failure. The strain distribution in the additive manufactured joints is uniformly distributed. However, the failure modes of tubular joints are similar, in which the transmission path from the upper brace to the lower brace is not direct.

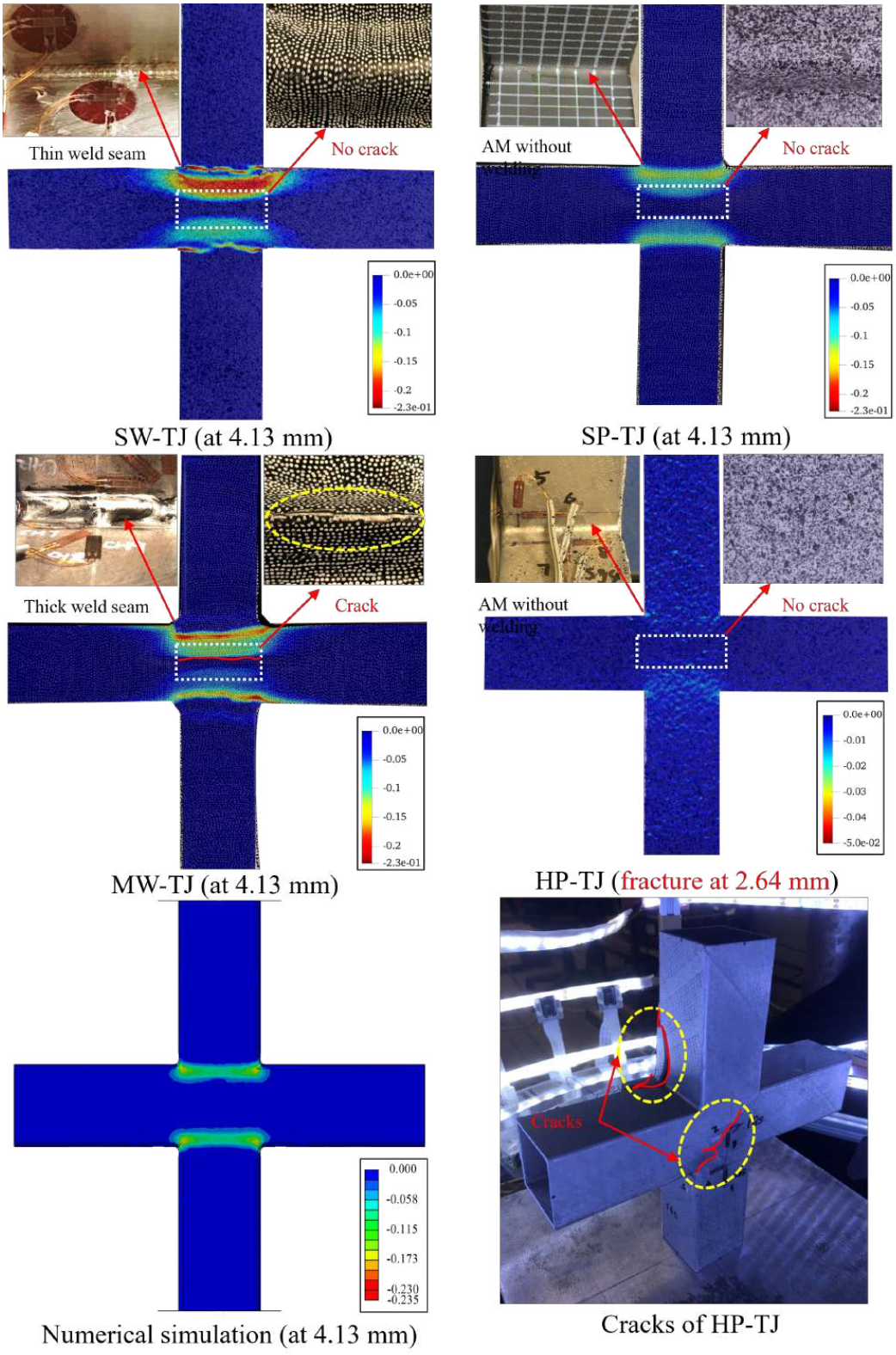

Figure 14: 2D-DIC results of different specimens and the numerical simulation.

4.2.2. *3D-DIC for optimized joints*

The 3D-DIC results for SP-REJ and HP-REJ under displacement-controlled loading when the vertical displacement is 3.8 mm and the corresponding numerical simulation outcomes are presented in Fig. 15. The material properties introduced in the numerical simulation are determined from the tensile test.

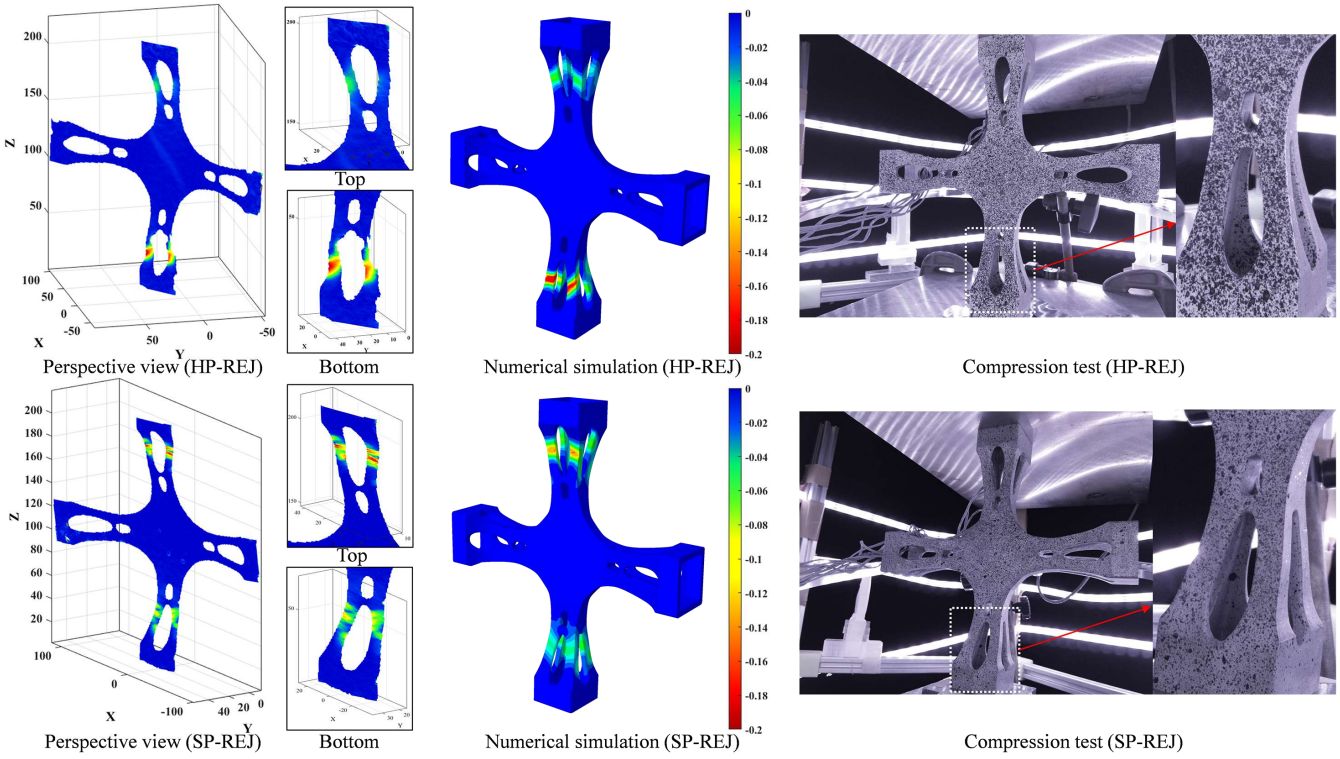

Figure 15: 3D-DIC results of different specimens and the numerical simulation (at 3.8 mm).

By comparing the results of 3D-DIC with those simulated by FEM at the same scale, the strain distributions in the vertical direction of the contour plots are all consistent. The 3D-DIC data provide a more intuitive monitoring of strain fluctuations during compression. The failure of the tubular joint at the center can lead to the failure of the entire joint which would affect all connected members. The innovative configuration of the optimized joint absorbs more deformation and energy, which allows the core region, i.e., the central part of the joint, to be protected from damage. The local buckling of the optimized joint prevents the failure of the whole joint, enabling the mechanism of strong-joint and weak-component

mechanism.

4.3. Load-displacement relationships

The Fig. 16 below depicts the relationship between the load and displacement of tubular joints and re-engineered joints made of various materials. Uniaxial compression tests are currently employed owing to the difficulty of the laboratory setup and the challenge of executing biaxial loads. The force transmission paths are independent when compressed in the two orthogonal directions because the optimized joints have symmetrical geometric features compared to the tubular joints. Although the HP material has the smallest fracture strain during the tensile test, the ultimate load of HP-TJ increases by 157.4 % compared to MW-TJ with the same failure modes, while HP-TJ fails at a vertical displacement of 2.7 mm. For the tubular joints MW-TJ and SW-TJ welded with different materials, the load-displacement relationships are approximately the same, but cracks appear on the sidewall of the chord at a vertical displacement of 4.13 mm for MW-TJ; however, no damages occur until 15 mm for SW-TJ from Fig. 14. SP-REJ and HP-REJ show significant increases of nearly 84.6 % and 161.5 % in the deformation associated with the maximum load compared to MW-TJ. The area enclosed by the load-displacement curve and coordinate axes are fuller for REJ than TJ, indicating that the joints can absorb more energy during the loading process. SP-REJ shows more stability without cracks compared to HP-REJ, and the ultimate load of HP-REJ is increased by 177.7 % compared to SP-REJ.

4.4. Validation of numerical simulations

The results of numerical simulations of tubular joints and optimized joints, which are additive manufactured with stainless steel and high-strength mold steel, are shown in Fig. 17. The ultimate loads of the simulation are consistent with that of experiments. Initial imperfections during compression and eccentric loading are the primary sources of errors. There is no significant difference in ultimate load between

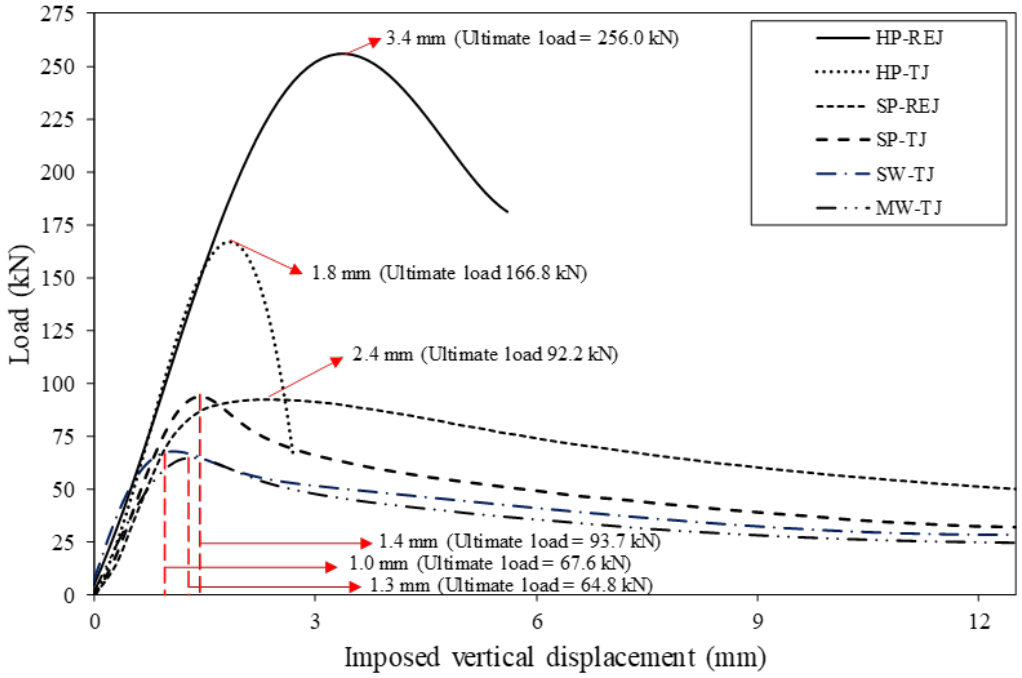

Figure 16: Load-displacement relationship of different joints.

tubular joints and re-engineered joints additively fabricated with stainless steel material; the main difference is reflected in the larger area of the plumper curve of the load-displacement relationship enclosed by the X-axis. It means that optimized joints with higher energy dissipation have the potential to improve the seismic resistance of the structural members. Furthermore, the reinforced HP material improves the mechanical properties of the optimized joint over the tubular joint, with a 53.5% increase in ultimate load.

4.5. Failure modes comparison

The sidewall deformation defines as the deformation in the horizontal direction at the center of the same position on the side surface of TJ or REJ. After comparing the horizontal displacement of the sidewall measured by LVDT in Fig. 18, it can be obtained that REJ and TJ are distributed on both sides of the line $y = x$. The mechanism of sidewall deformation under vertical compression is different for TJ and REJ. The lateral displacement of TJ is larger than the vertical displacement, which means that the vertical loading will affect the other connected members if they are also connected laterally. When vertical

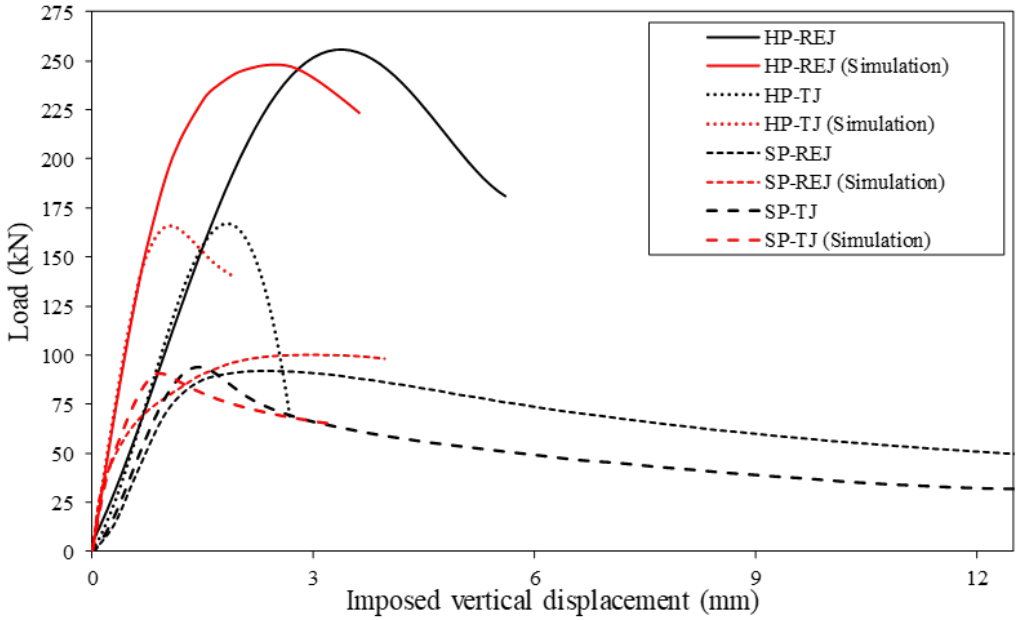

Figure 17: Numerical simulation for 3D printed joints.

loading is applied, the innovative features of the edge part of REJ can effectively absorb the energy and thus reduce the horizontal displacement at the center, which implies that there is less effect on the other connected members when the joint is loaded vertically.

When investigating the core region of deformation from the strain gauge measurements, the results of TJ and REJ are shown as Figs. 19 and 20, respectively. Failure mechanisms are similar for MW-TJ, SW-TJ, and SP-TJ joints, with failure occurring at the sidewalls and indentations on the upper and lower surfaces of the chord; however, there is no damage at the upper and lower braces. As for HP-TJ, the lateral sidewall displacement during vertical compression leads to tensile cracks at the corners between the sidewall and the upper and lower surfaces, resulting in limited ductility of the 3D printed tubular joints. For topology-optimized joints manufactured by 3D printing, the innovative region near the boundary can absorb energy and deform as much as possible to ensure the integrity of the overall joint and avoid the problem of limited ductility induced by local cracking. The mechanical behavior of the topology-optimized joint can be entirely enhanced by avoiding the fracture-prone features of HP as much

as possible.

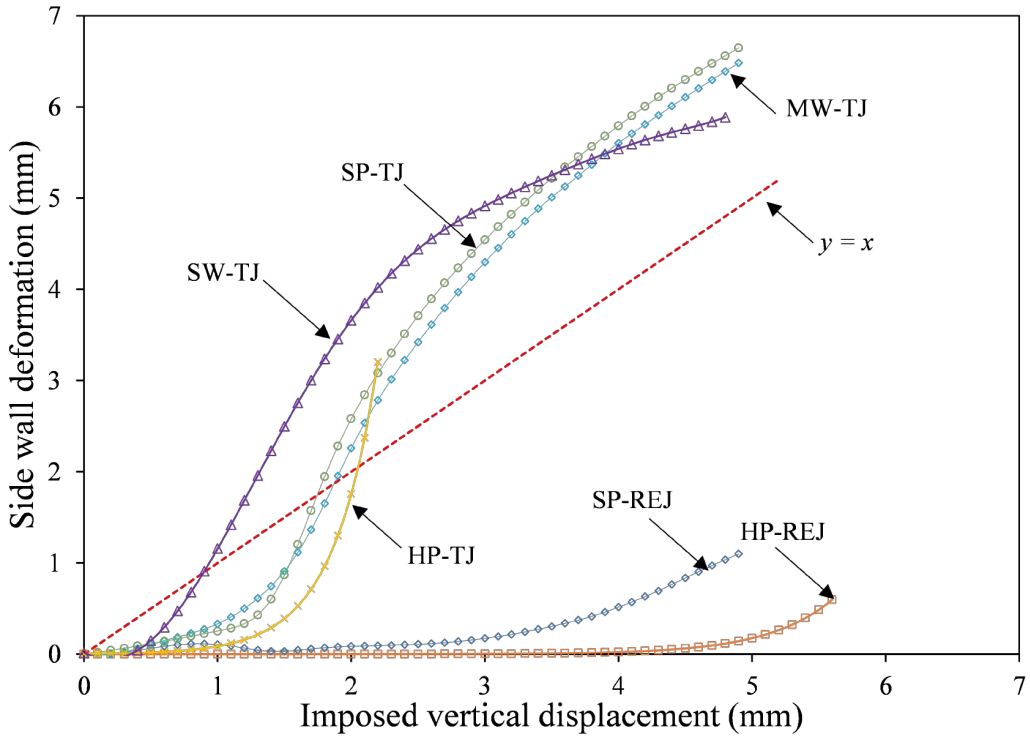

Figure 18: Side wall deformation vs. imposed vertical displacement of different joints.

5. Conclusions and future work

SIMP is implemented in this paper to optimize the steel joints. And three materials, conventional mild steel (MW), stainless steel (SW & SP), and high-strength mold steel (HP), are employed for welding and 3D printing to fabricate tubular joints and optimized joints. The application of non-contact 2D and 3D-DIC, validated by numerical simulations, enables accurate strain measurement on joint surfaces of arbitrary geometry. The following are the main conclusions obtained:

(1) The optimized joint can reduce the maximum stress by 58.5% compared with the tubular joint under the same boundary conditions and loads in numerical simulation, as long as the optimization constraints are satisfied. The stress distribution of the optimized joint is more uniform to avoid stress concentration.

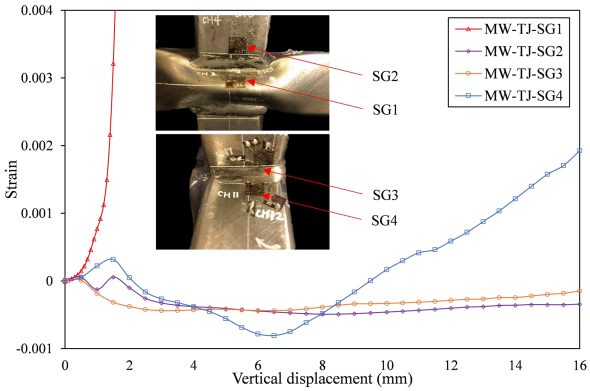

(a) Strain distribution of MW-TJ.

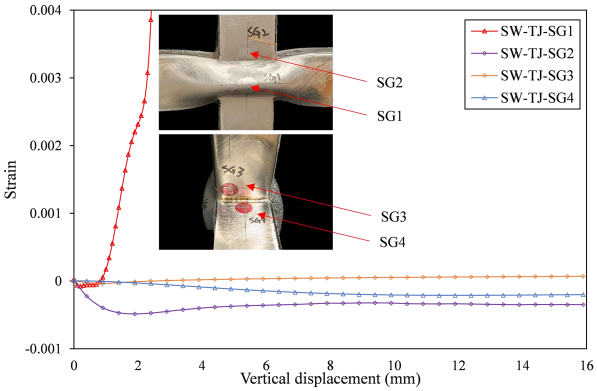

(b) Strain distribution of SW-TJ.

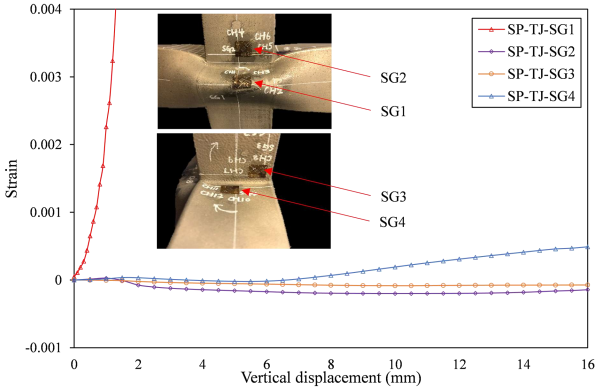

(c) Strain distribution of SP-TJ.

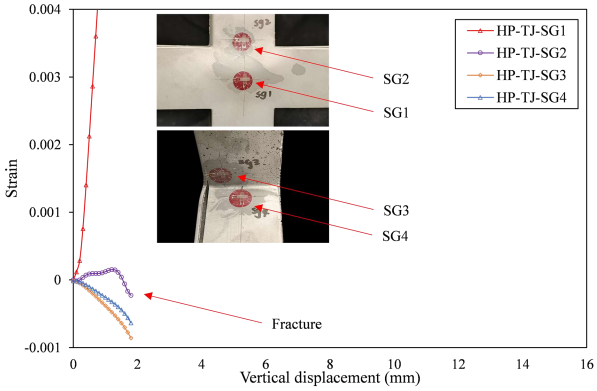

(d) Strain distribution of HP-TJ.

Figure 19: Gauges results of tubular joints.

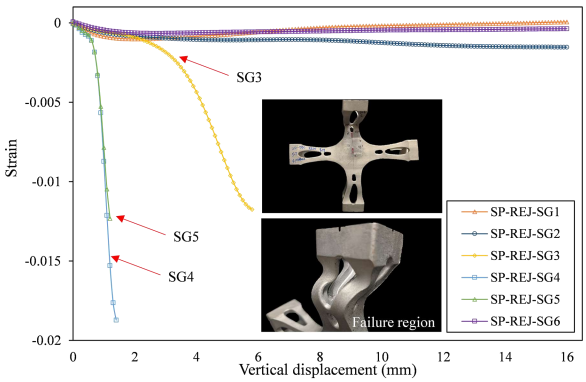

(a) Strain distribution of SP-REJ.

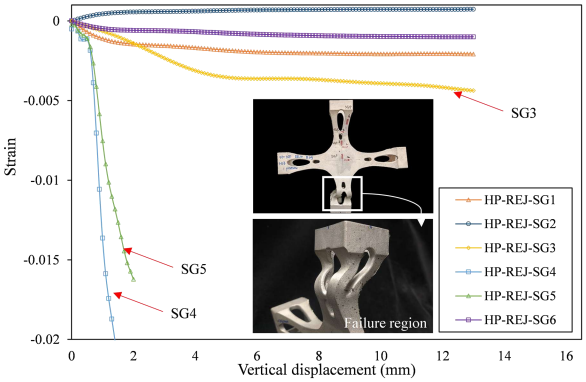

(b) Strain distribution of HP-REJ.

Figure 20: Gauge results of optimized joints.

(2) From the results of material tensile tests, SW cut from cold rolled stainless steel tubes has stable material properties and which is suitable for welding. Young's modulus of MW is the largest, and it varies widely in terms of fracture strain. The stability of materials such as SP and HP can be well controlled during additive manufacturing. The yield strength and ultimate strength of HP are significantly greater than that of SP, but the elongation at fracture of HP is the smallest.

(3) Additive manufacturing allows the production of more accurate joints. Removing the weld seam can also avoid defects such as cracks, porosity, and slag, which can lead to stress concentrations and poor quality of joints when welding. HP would generate cracks suddenly, making it less suitable for manufacturing tubular joints when compared to SP. The strain distribution in 3D printed tubular joints is more uniform compared to welded tubular joints. The failure modes of the tubular joints are similar in the connection regions between the brace and the chord, where the load is transferred indirectly from the upper brace to the chord sidewall and then to the lower brace. Nevertheless, the failure modes of the re-engineered joints after optimization have changed. The innovative configuration of the optimized joint absorbed more energy, which resulted in the protection of the central core region of the joint.

(4) The results of 2D-DIC and 3D-DIC allow more visual observation of the strain distribution during the compression test, which is validated through numerical simulations, demonstrating its high applicability to experiments with joints of arbitrary geometrical configurations after optimization.

(5) Under the same failure modes, HP-TJ showed the most significant increase in ultimate load but failed only when the imposed displacement reaches 2.7 mm. The load-displacement relationship and sidewall deformation for welded tubular joints with various materials like SW-TJ and MW-TJ are generally the same. However, cracks appeared in the side walls of the chord when MW-TJ at a vertical displacement of 4.13 mm. There are still some challenges or limitations in the ductility of the joint

manufactured with the material of high-strength mold steel, which must be applied in the appropriate sites despite its extreme yield strength. The advent of topology optimization technique allows to design the new forms of joints with more reasonable material distributions, which can further improve the ductility of the entire high-strength steel structures to avoid brittle damage.

Topology-optimized joints achieve strong-joint and weak-component mechanism that enables high-strength steels to maintain ductility by taking full advantage of the high yield strength. Moreover, topology optimization combined with additive manufacturing allows independent fabrication of the joints avoiding on-site welding, ensuring higher strength, and preventing stress concentration and defects such as cracks, porosity, and slag. It can be considered as a reliable alternative to the conventional welded joints for the innovative customized building components in the future. Also, other constraints such as material plasticity should be introduced into the optimization framework. Besides, optimization of joints with different geometrical configurations, such as T-joints and multi-planar spatial joints, will be carried out. And wire arc additive manufacturing (WAAM) method will be considered for exploring the topology optimization of large-scale joints.

6. Acknowledgement

We are thankful to Dr. J. He and Dr. Y.C. Cai. for their friendly assistance in the research work on numerical simulation and experiments. This work is generously supported by the Research Grants Council via RGC/CRF (C7038-20GF) and RGC/GRF (17204122), Shenzhen Science and Technology Innovation Committee via Shenzhen-Hong Kong-Macau Technology Research Program (Type C, SGDX-2020110309280100) and Fundamental Research General Program (2021302011), and National Natural Science Foundation of China via General Program (Project No. 51878586).

References

[1] Y. Chen, R. Feng, C. Wang, Tests of steel and composite chs x-joints with curved chord under axial compression, Engineering Structures 99 (2015) 423–438.

[2] W. Li, S. Zhang, W. Huo, Y. Bai, L. Zhu, Axial compression capacity of steel chs x-joints strengthened with external stiffeners, Journal of Constructional Steel Research 141 (2018) 156–166.

[3] W. Zhang, Y. S. Choo, P. Yang, W. Shen, Z. Huang, Nonlinear behaviour of fully grouted chs x joints and associated representation for overall frame analysis, Thin-Walled Structures 152 (2020) 106761.

[4] K. Yang, L. Zhu, Y. Bai, H. Sun, M. Wang, Strength of external-ring-stiffened tubular x-joints subjected to brace axial compressive loading, Thin-Walled Structures 133 (2018) 17–26.

[5] L. Zhu, Q. Song, Y. Bai, Y. Wei, L. Ma, Capacity of steel chs t-joints strengthened with external stiffeners under axial compression, Thin-Walled Structures 113 (2017) 39–46.

[6] Z. Yang, H. Deng, X. Hu, Strength of longitudinal x-type plate-to-circular hollow section (chs) connections reinforced by external ring stiffeners, Thin-Walled Structures 131 (2018) 500–518.

[7] L. Tong, G. Xu, X.-L. Zhao, Y. Yan, Fatigue tests and design of cfrp-strengthened chs gap k-joints, Thin-Walled Structures 163 (2021) 107694.

[8] P. Collin, B. Johansson, Bridges in high strength steel, IABSE REPORTS 92 (2006) 434.

[9] G. Shi, F. Hu, Y. Shi, Recent research advances of high strength steel structures and codification of design specification in china, International Journal of Steel Structures 14 (4) (2014) 873–887.

[10] H. Ban, G. Shi, A review of research on high-strength steel structures, Proceedings of the Institution of Civil Engineers-Structures and Buildings 171 (8) (2018) 625–641.

[11] G. Shi, H. Ban, Y. Bai, Y. Wang, C. Luo, Y. Shi, A novel cast aluminum joint for reticulated shell structures: experimental study and modeling, Advances in Structural Engineering 16 (6) (2013) 1047–1059.

[12] J. L. Jewett, J. V. Carstensen, Topology-optimized design, construction and experimental evaluation of concrete beams, Automation in Construction 102 (2019) 59–67.

[13] D. Jankovics, A. Barari, Customization of automotive structural components using additive manufacturing and topology optimization, IFAC-PapersOnLine 52 (10) (2019) 212–217.

[14] J.-H. Zhu, W.-H. Zhang, L. Xia, Topology optimization in aircraft and aerospace structures design, Archives of Computational Methods in Engineering 23 (4) (2016) 595–622.

[15] S. Guanghui, G. Chengqi, Q. Dongliang, W. Dongtao, T. Lei, G. Tong, An aerospace bracket designed by thermo-elastic topology optimization and manufactured by additive manufacturing, Chinese Journal of Aeronautics 33 (4) (2020) 1252–1259.

[16] J. D. Deaton, R. V. Grandhi, A survey of structural and multidisciplinary continuum topology optimization: post 2000, Structural and Multidisciplinary Optimization 49 (1) (2014) 1–38.

[17] X. Guo, G.-D. Cheng, Recent development in structural design and optimization, Acta Mechanica Sinica 26 (6) (2010) 807–823.

[18] Y. M. Xie, G. P. Steven, A simple evolutionary procedure for structural optimization, Computers & structures 49 (5) (1993) 885–896.

[19] M. P. Bendsøe, Optimal shape design as a material distribution problem, Structural optimization 1 (4) (1989) 193–202.

[20] Z. Jihong, Z. Han, W. Chuang, Z. Lu, Y. Shangqin, W. Zhang, A review of topology optimization for additive manufacturing: Status and challenges, Chinese Journal of Aeronautics 34 (1) (2021) 91–110.

[21] T. P. Ribeiro, L. F. Bernardo, J. M. Andrade, Topology optimisation in structural steel design for additive manufacturing, Applied Sciences 11 (5) (2021) 2112.

[22] S. Galjaard, S. Hofman, S. Ren, New opportunities to optimize structural designs in metal by using additive manufacturing, in: Advances in architectural geometry 2014, Springer, 2015, pp. 79–93.

[23] Z. Li, K. D. Tsavdaridis, L. Gardner, A review of optimised additively manufactured steel connections for modular building systems, Industrializing Additive Manufacturing: Proceedings of AMPA2020 (2021) 357–373.

[24] J. Lange, T. Feucht, M. Erven, 3d printing with steel: Additive manufacturing for connections and structures, Steel Construction 13 (3) (2020) 144–153.

[25] H. Seifi, A. R. Javan, X. Lin, Y. M. Xie, An innovative and inexpensive experimental setup for testing connections in gridshell structures, Engineering Structures 207 (2020) 110257.

[26] C. Bañón, F. Raspall, C. BAÑÓN, F. RASPALL, Optimized structures: Airmesh, 3D Printing Architecture: Workflows, Applications, and Trends (2021) 21–37.

[27] M. Seabra, J. Azevedo, A. Araújo, L. Reis, E. Pinto, N. Alves, R. Santos, J. P. Mortágua, Selective laser melting (slm) and topology optimization for lighter aerospace componentes, Procedia Structural Integrity 1 (2016) 289–296.

[28] A. Paolini, S. Kollmannsberger, E. Rank, Additive manufacturing in construction: A review on processes, applications, and digital planning methods, Additive manufacturing 30 (2019) 100894.

[29] M. Javaid, A. Haleem, Additive manufacturing applications in medical cases: A literature based review, Alexandria Journal of Medicine 54 (4) (2018) 411–422.

[30] M. A. Sutton, J. J. Orteu, H. Schreier, Image correlation for shape, motion and deformation measurements: basic concepts, theory and applications, Springer Science & Business Media, 2009.

[31] D. Solav, K. M. Moerman, A. M. Jaeger, K. Genovese, H. M. Herr, Multidic: An open-source toolbox for multi-view 3d digital image correlation, IEEE Access 6 (2018) 30520–30535. doi:10.1109/ACCESS.2018.2843725.

[32] B. Pan, K. Qian, H. Xie, A. Asundi, Two-dimensional digital image correlation for in-plane displacement and strain measurement: a review, Measurement science and technology 20 (6) (2009) 062001.

[33] F. Hild, S. Roux, Digital image correlation: from displacement measurement to identification of elastic properties–a review, Strain 42 (2) (2006) 69–80.

[34] M. Palanca, G. Tozzi, L. Cristofolini, The use of digital image correlation in the biomechanical area: a review, International biomechanics 3 (1) (2016) 1–21.

[35] K. Genovese, L. Casaletto, J. D. Humphrey, J. Lu, Digital image correlation-based point-wise inverse characterization of heterogeneous material properties of gallbladder in vitro, Proceedings of the Royal Society A: Mathematical, Physical and Engineering Sciences 470 (2167) (2014) 20140152.

[36] P. Badel, S. Avril, S. Lessner, M. Sutton, Mechanical identification of layer-specific properties of

mouse carotid arteries using 3d-dic and a hyperelastic anisotropic constitutive model, Computer methods in biomechanics and biomedical engineering 15 (1) (2012) 37–48.

[37] S. Avril, Hyperelasticity of soft tissues and related inverse problems, in: Material parameter identification and inverse problems in soft tissue biomechanics, Springer, 2017, pp. 37–66.

[38] A. Dickinson, A. Taylor, H. Ozturk, M. Browne, Experimental validation of a finite element model of the proximal femur using digital image correlation and a composite bone model, Journal of biomechanical engineering 133 (1).

[39] R. Maiti, L.-C. Gerhardt, Z. S. Lee, R. A. Byers, D. Woods, J. A. Sanz-Herrera, S. E. Franklin, R. Lewis, S. J. Matcher, M. J. Carré, In vivo measurement of skin surface strain and sub-surface layer deformation induced by natural tissue stretching, journal of the mechanical behavior of biomedical materials 62 (2016) 556–569.

[40] K. Ito, K. Maeda, I. Fujiwara, K. Hosoda, T. Nagura, T. Lee, N. Ogihara, Dynamic measurement of surface strain distribution on the foot during walking, Journal of the mechanical behavior of biomedical materials 69 (2017) 249–256.

[41] V. Laghi, M. Palermo, G. Gasparini, V. A. Girelli, T. Trombetti, On the influence of the geometrical irregularities in the mechanical response of wire-and-arc additively manufactured planar elements, Journal of Constructional Steel Research 178 (2021) 106490. doi:https://doi.org/10.1016/j.jcsr.2020.106490.

[42] C. Huang, P. Kyvelou, R. Zhang, T. Ben Britton, L. Gardner, Mechanical testing and microstructural analysis of wire arc additively manufactured steels, Materials & Design 216 (2022) 110544. doi:https://doi.org/10.1016/j.matdes.2022.110544.

[43] V. Laghi, L. Tonelli, M. Palermo, M. Bruggi, R. Sola, L. Ceschini, T. Trombetti, Experimentally-validated orthotropic elastic model for wire-and-arc additively manufactured stainless steel, Additive Manufacturing 42 (2021) 101999. doi:https://doi.org/10.1016/j.addma.2021.101999.

[44] M. P. Bendsøe, O. Sigmund, Material interpolation schemes in topology optimization, Archive of applied mechanics 69 (9) (1999) 635–654.

[45] O. Sigmund, Design of material structures using topology optimization, Ph.D. thesis, Technical University of Denmark Denmark (1994).

[46] O. Sigmund, J. Petersson, Numerical instabilities in topology optimization: a survey on procedures dealing with checkerboards, mesh-dependencies and local minima, Structural optimization 16 (1) (1998) 68–75.

[47] T. E. Bruns, D. A. Tortorelli, Topology optimization of non-linear elastic structures and compliant mechanisms, Computer methods in applied mechanics and engineering 190 (26-27) (2001) 3443–3459.

[48] M. Pandey, B. Young, Structural performance of cold-formed high strength steel tubular x-joints under brace axial compression, Engineering Structures 208 (2020) 109768.

[49] R. Feng, B. Young, Stress concentration factors of cold-formed stainless steel tubular x-joints, Journal of Constructional Steel Research 91 (2013) 26–41.

[50] X. Lan, T.-M. Chan, B. Young, Static strength of high strength steel chs x-joints under axial compression, Journal of Constructional Steel Research 138 (2017) 369–379.

[51] CIDECT, Design guide for rectangular hollow section joints under predominantly static loading.,

Second Edition, Comité International pour Ie Développement et l'Étude de la Construction Tubulaire, LSS Verlag, Dortmund, Germany.

[52] E. 3, Design of steel structures—part 1–8: Design of joints., European Committee for Standardization, EN 1993-1-8, CEN. Brussels, Belgium.

[53] S. Huang, X. Deng, L. K. Lam, Integrated design framework of 3d printed planar stainless tubular joint: Modelling, optimization, manufacturing, and experiment, Thin-Walled Structures 169 (2021) 108463. doi:https://doi.org/10.1016/j.tws.2021.108463.

[54] D. Turner, Digital image correlation engine (dice) reference manual, Sandia Report o (10606).

[55] Y. Dong, B. Pan, A review of speckle pattern fabrication and assessment for digital image correlation, Experimental Mechanics 57 (8) (2017) 1161–1181.

[56] P. Zhou, K. E. Goodson, Subpixel displacement and deformation gradient measurement using digital image/speckle correlation, Optical Engineering 40 (8) (2001) 1613–1620.

[57] B. J. Murienne, T. D. Nguyen, A comparison of 2d and 3d digital image correlation for a membrane under inflation, Optics and lasers in engineering 77 (2016) 92–99.

[58] B. Pan, L. Yu, Q. Zhang, Review of single-camera stereo-digital image correlation techniques for full-field 3d shape and deformation measurement, Science China Technological Sciences 61 (1) (2018) 2–20.

[59] Y. I. Abdel-Aziz, H. M. Karara, M. Hauck, Direct linear transformation from comparator coordinates into object space coordinates in close-range photogrammetry, Photogrammetric engineering & remote sensing 81 (2) (2015) 103–107.

[60] W. Meiners, K. Wissenbach, A. Gasser, Shaped body especially prototype or replacement part production, DE Patent 19.

[61] E.-. ASTM, et al., Standard test methods for tension testing of metallic materials, Annual book of ASTM standards. ASTM.

[62] Y. Huang, B. Young, The art of coupon tests, Journal of Constructional Steel Research 96 (may) (2014) 159–175.

Appendix A. Abbreviations

TO	Topology optimization
SIMP	Solid isotropic material with penalization method
AM	Additive manufacturing
MW	Mild steel by welding
SW	Stainless steel by welding
SP	Stainless steel by 3D printing
HP	High-strength mold steel by 3D printing
TJ	Tubular joint
REJ	Re-engineered joint after optimization
2D / 3D-DIC	2D/3D digital image correlation method
SG	Strain gauge
LVDT	Linear variable differential transformer
ROI	Region of interest
FOV	Field of view